Inhibitory Effect of Magnesium and Zinc on Crystallization Kinetics of Hydroxyapatite (0001) Face

Noriko Kanzaki,[†] Kazuo Onuma,*[,‡] Gabin Treboux,[‡] Sadao Tsutsumi,[†] and Atsuo Ito[‡]

School of Science and Engineering, Waseda University, 1-6-1 Nishiwaseda, Shinjuku-ku, Tokyo, 169-8050 Japan, and National Institute for Advanced Interdisciplinary Research, MITI, 1-1-4 Higashi, Tsukuba-shi, Ibaraki, 305-8562 Japan

Received: November 9, 1999; In Final Form: February 1, 2000

The effect of magnesium and zinc on the growth kinetics of a hydroxyapatite (0001) face in pseudophysiological solutions was investigated. The growth rates of the (0001) face were measured under various concentrations of magnesium or zinc using Moire phase shift interferometry coupled with surface observation by atomic force microscopy. The (0001) face grew not in a spiral growth mode but in a multiple two-dimensional nucleation growth mode. It was shown that the lateral growth of two-dimensional islands on the (0001) face was inhibited by the addition of magnesium or zinc, following an inhibition of the normal growth rate of the face. Although both cations inhibited growth, zinc was found to reduce the growth rate about 1000 times more effectively than magnesium.

Introduction

It is important to clarify the effect of trace elements on the growth mechanism of hydroxyapatite ($Ca_{10}(PO_4)_6(OH)_2$; HAP), an inorganic component of human bone and tooth, for correct understanding of the biomineralization process. In vivo, HAP grows in a solution which contains many essential trace elements besides calcium and phosphorus. Among these essential trace elements, magnesium and zinc have a great influence on the growth kinetics of HAP. For instance, it is well-known that magnesium inhibits phase transformation from amorphous calcium phosphate to HAP.[1,2] From the viewpoint of bone-cell biology, zinc is known to promote bone formation by stimulating osteoblasts which are cells that produce bone HAP.[3,4] Zinc-containing calcium phosphate implants have been found to have a stimulant effect on bone formation.[5] However, an elevated amount of zinc might inhibit the growth of bone HAP.

Indeed, inhibitory effects of magnesium and zinc on HAP crystal growth have been investigated, for example, such as a dual constant composition (DCC) method.[6−8] It was confirmed that magnesium and zinc reduced the growth rate of HAP. However, the previous method did not discriminate between the growth rates of $(10\bar{1}0)$, *a*- and (0001), *c*-faces despite the high precision associated with the method. Moreover, surface observation of grown crystals was not performed in the previous studies although much information can be obtained through surface observation. It is thus necessary to measure the growth rate of each face separately with surface observation, using single-crystal HAP as a seed, to obtain more detailed information about the inhibitory effects. HAP crystal is bounded by *a*- and *c*-faces and has large anisotropy. Biologically, the inhibitory effects on the *c*-face are more important than that on the *a*-face since biological HAP grows mainly in the *c*-direction.[9]

In the present study, we performed direct growth rate measurements of the *c*-face in the presence of magnesium and zinc in pseudophysiological solutions. Moire phase shift interferometry was employed for the precise measurement of growth rates coupled with surface observation by atomic force microscopy (AFM). The growth rates obtained were analyzed using theoretical equations of adsorption isotherms.

Experimental Section

1. HAP Seed Crystals. The seed crystals used in the present study were hydrothermally synthetic HAP single crystals bounded by *a*- and *c*-faces.[10] The size of the seed crystals was 1−4 mm and 20−50 μm along the *c*- and *a*-directions, respectively. Single crystals were used after masking *a*-faces with epoxy resin for all experiments so that only one *c*-face grows.

2. Pseudophysiological Solutions. The pseudophysiological solutions contain 140 mM NaCl, 1.0 mM $K_2HPO_4{\cdot}3H_2O$, 2.5 mM $CaCl_2$, and either 0−1.5 mM $MgCl_2{\cdot}6H_2O$ or 0−7.5 μM $ZnCl_2$. The pseudophysiological solutions were prepared using extrapure-grade reagents (Nacalai Tesque, Inc., Tokyo, Japan) and ultrapure CO_2-free water, and were buffered at pH 7.4 by tris-(hydroxymethyl)aminomethane and 1 N HCl at 25 °C. Supersaturation of the solutions was 22.0 with respect to HAP, as calculated from

$$\sigma = (I_p/K_{sp})^{1/18} - 1 \qquad (1)$$

where I_p and K_{sp} are the ionic product and solubility product, respectively. I_p was calculated using the dissociation constants described elsewhere.[11] The activity coefficients were calculated using the Debye−Huckel limiting law.[12] A K_{sp} value of 10^{-119} was used in the present study.

3. Moire Phase Shift Interferometry. Moire phase shift interferometry was used to measure growth rates of the *c*-face. Common-path two-beam interferometry with a Nomarsky prism was used to eliminate mechanical disturbance (Figure 1).[13,14] The interferometry used has a theoretical accuracy with 0.5 nm

* To whom correspondence should be addressed: National Institute for Advanced Interdisciplinary Research, Cell Tissue Module Group, 1-1-4 Higashi, Tsukuba-shi, Ibaraki, 305-8562 Japan. Tel.: +81−298−61−2557. Fax: +81-298-61-2565. E-mail: onuma@nair.go.jp.

[†] School of Science and Engineering, Waseda University.

[‡] National Institute for Advanced Interdisciplinary Research.

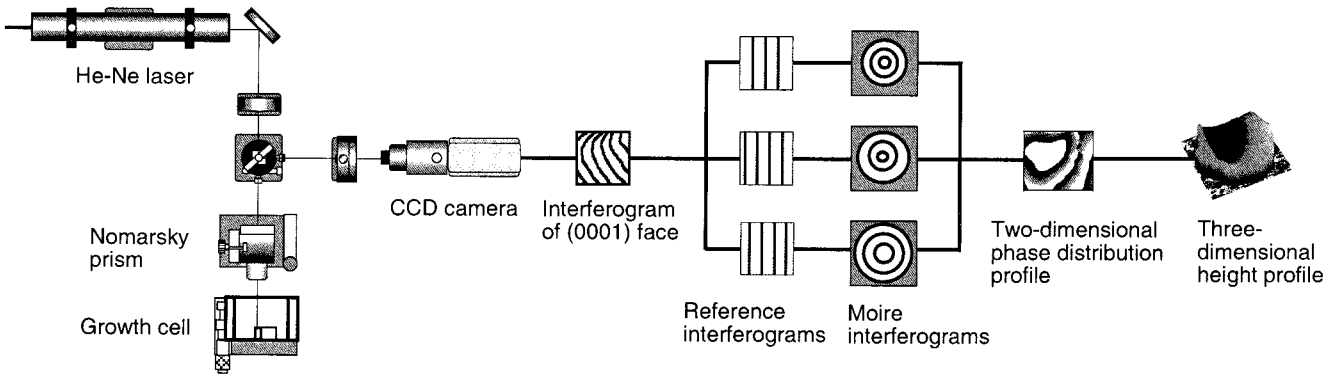

Figure 1. Schematic drawing of common-path two-beam interferometry and a signal processing route using Moire phase shift technique. A two-dimensional phase distribution profile is constructed from an interferogram of *c*-face in real time.

in height resolution. The process for reconstructing a three-dimensional height profile of the *c*-face from the interferogram is as follows. Three reference interferograms with phase shifts of $\pi/2$ to each other are digitally composed in a signal processor as carrier fringes. Three Moire interferograms of intensity I_j ($j = 1$, 2, or 3) are created between the interferogram of the *c*-face and the three reference interferograms. These three Moire interferograms also have phase shifts of $\pi/2$ to each other. A two-dimensional phase distribution profile, $\phi(x,y)$, on the *c*-face is calculated using

$$\phi(x,y) = \tan^{-1}[(I_3 - I_2)/(I_1 - I_2)] + \pi/4 \qquad (2)$$

and is related to the three-dimensional height profile $h(x,y)$ as

$$h(x,y) = \phi(x,y)\lambda/4\pi n \qquad (3)$$

where λ and n are the wavelength of the laser and the refractive index of the solution, respectively. Therefore, the growth rate at a certain point on the *c*-face can be calculated from the change in the three-dimensional height profile, with time. All processes described above are finished in 1/30 s real time. Growth rates were measured at 25 ± 1 °C.

4. Surface Observation. The seed crystals were immersed in the pseudophysiological solutions for 4 h at 25 °C after being etched in a 1 N HCl solution. After the immersion, the crystals were immediately washed with ultrapure water, and the surface morphology of the *c*-face was observed using a NanoScope III-a AFM (Digital Instruments, Inc.). A tapping mode was employed for all the observations using silicon cantilevers with a spring constant of 20−50 N/m and a J-type (100 μm scanning range) piezo scanner.

Results

1. Growing Phase. Growing phase at magnesium concentrations of 0.045 and 1.5 mM was identified using a micro-Raman spectroscopy, since it has been reported that whitlockite, having resemblance to β-TCP, $Ca_3(PO_4)_2$, could grow under a room temperature in magnesium containing solutions.[15] The intense peaks for HAP corresponding to the PO_4^{3-} tetrahedron ($\nu 1$ symmetric stretching vibration) around 962 cm^{-1} and the O−H stretching vibration around 3576 cm^{-1} were reported.[16] The wavenumbers of center positions for $\nu 1$ peaks were observed at 960.8, 961.1, and 961.7 cm^{-1} for seed, growing phase at magnesium concentration of 0.045 and 1.5 mM, respectively. However, peaks for whitlockite which should appear around 966 and 408 cm^{-1} were not detected on growing phase.[17] The

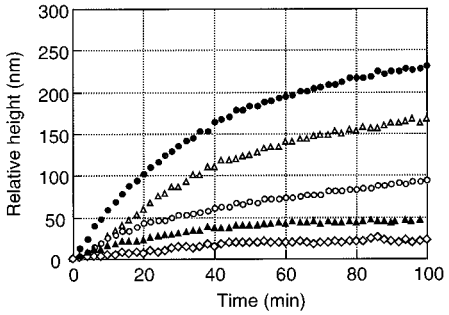

Figure 2. Relative height as a function of time on the *c*-face at concentrations of (●) 0.03 mM magnesium, (△) 0.3 μM zinc, (○) 0.75 μM zinc, (▲) 0.75 mM magnesium, and (◇) 4.5 μM zinc.

2. Growth Rate Measurement. Diminishing growth rates with time were observed in all growth rate measurements regardless of the concentration of either magnesium or zinc (Figure 2). The growth rates diminished more quickly with an increase of concentrations of magnesium and zinc. This phenomenon was also observed in the solution without impurities and never due to decreasing supersaturation of the solutions during the growth. The reason of diminishing growth rates with time may be a strain accumulation caused by a structural mismatch between the seed surface and the grown layer, as suggested in our previous paper.[13] The structural mismatch occurs because the crystallinity of the grown layer is lower than that of seed crystal. The strain accumulation proceeds during the growth and increases chemical potential of a bulk crystal following the decrease of driving force for the growth, although the supersaturation of the solution remains constant. It is expected that the high concentration of magnesium or zinc introduces defects in a structure of the grown layer and increases strain accumulation. The growth rate approached nearly zero after 4 h of growth although the supersaturation remained unchanged with respect to HAP. Since the growth rate strongly depended on time, the initial growth rates at $t = 0$ were used to represent the overall growth rates in the following analysis. The initial growth rate was calculated from the slope of the tangent line at $t = 0$ of a fifth-order polynomial function fitted to the measured data.

Zinc inhibited the growth of the *c*-face about 1000 times more effectively than magnesium (Figure 3). Zinc addition at a concentration of 1.5 μM decreased the growth rate by 70% whereas a magnesium concentration of 1.5 mM is required to decrease the growth rate to the same level. Zinc inhibited the growth of the *c*-face more completely than magnesium (Figure 3). Zinc reduced the growth rate by 90% at the highest

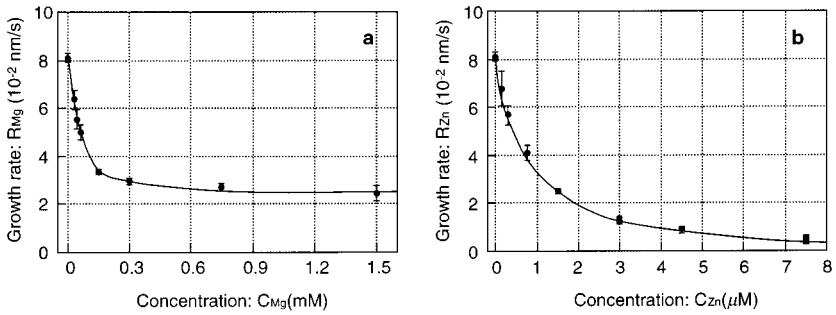

Figure 3. Growth rate of *c*-face as a function of impurity concentration (a) in the presence of magnesium and (b) in the presence of zinc.

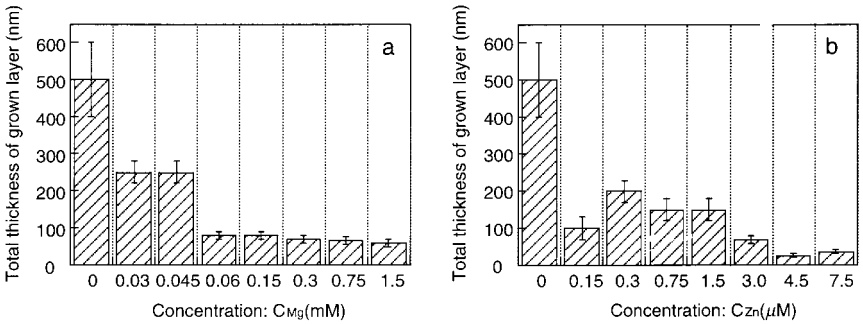

Figure 4. Total thickness of grown layer as a function of impurity concentration (a) in the presence of magnesium and (b) in the presence of zinc.

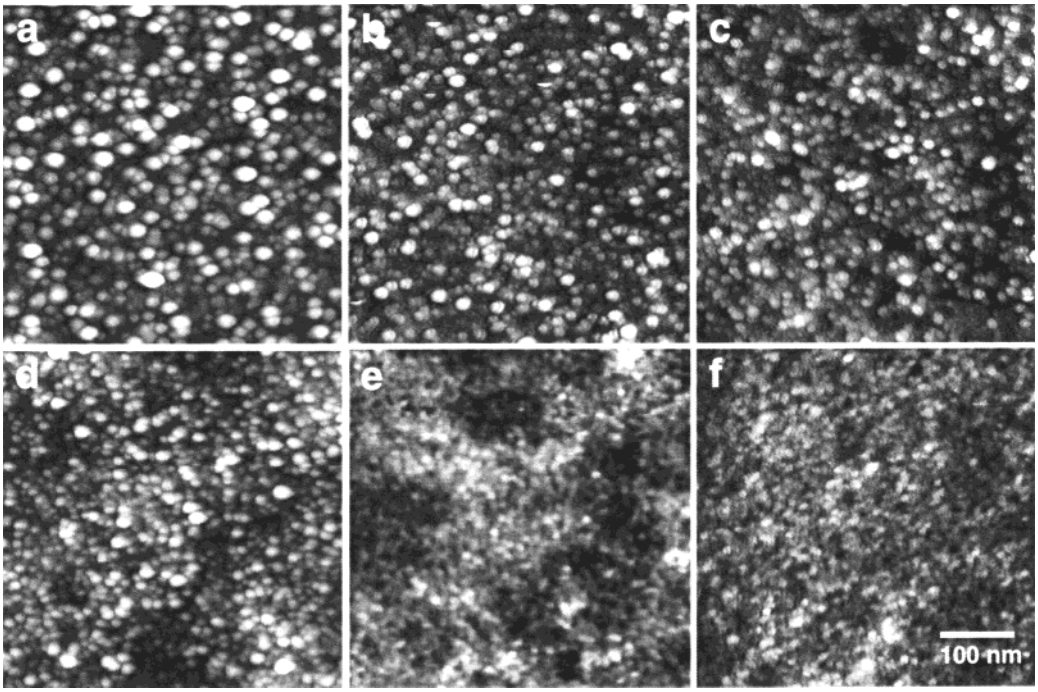

Figure 5. AFM images of *c*-faces after 4 h of growth at concentrations of (a) 0.03 mM magnesium, (b) 0.3 mM magnesium, (c) 1.5 mM magnesium, (d) 0.3 μM zinc (e) 1.5 μM zinc, and (f) 7.5 μM zinc.

grown layer ultimately decreased by about 95 and 80% with the presence of zinc and magnesium, respectively (Figure 4).

3. Surface Observation. The growth of the *c*-face proceeded in a multiple two-dimensional nucleation mode (Figure 5). No spiral growth was observed. Even in the presence of magnesium or zinc, this growth feature was unchanged, except for a decrease in the diameter of two-dimensional islands. It was found that zinc reduced the diameter more effectively and completely than magnesium (Figure 6), as in the result of growth rate measurement (Figure 3). Therefore, zinc more strongly inhibits the lateral growth of two-dimensional islands than magnesium.

the nucleation rate J can be assumed to be constant regardless of the magnesium or zinc concentration in the measured range at the present supersaturation with respect to HAP.

4. Models for Impurity Adsorption. The relationship between the growth rate and the concentration of magnesium or zinc was analyzed using Langmuir and Temkin adsorption isotherms. When an impurity, either magnesium or zinc, poisons active growth sites on the *c*-face, the coverage by impurities, θ, for each adsorption model is described by

$$\theta = KC_i/(1 + KC_i), \quad \text{Langmuir isotherm} \qquad (4)$$

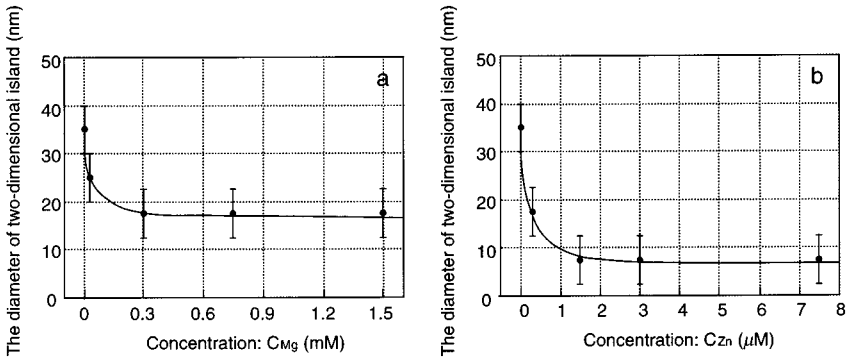

Figure 6. The diameter of two-dimensional islands nucleated on the *c*-face as a function of impurity concentration (a) in the presence of magnesium and (b) in the presence of zinc.

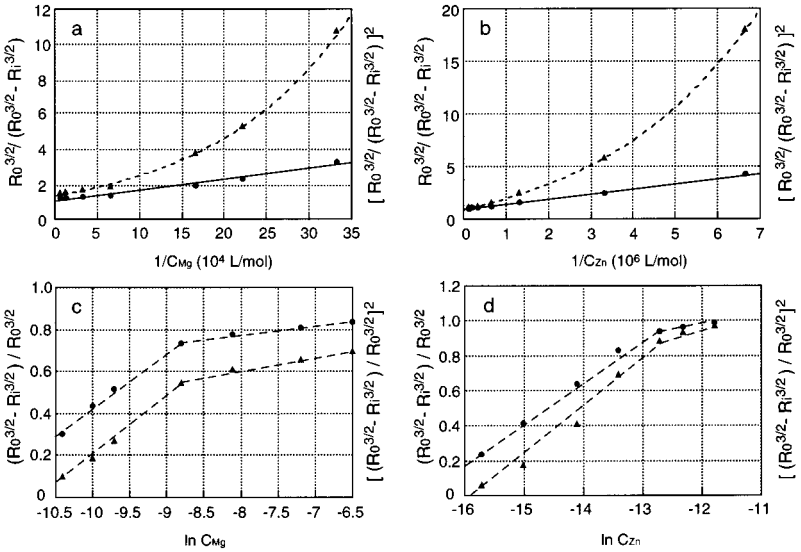

Figure 7. (a) Langmuir plots and (b) Temkin plots; (●) kink model, (▲) terrace model.

where K and C_i are the adsorption constant for the Langmuir isotherm and an impurity concentration, respectively; C_0 and Z are the adsorption constant for the Temkin isotherm and a constant, respectively. The θ affects the step velocity differently depending on whether the adsorption site is a kink of a step front or a surface terrace. When the adsorption site is the kink site, the step velocity is related to the impurity concentration as[18−19]

$$v_0/(v_0 - v_i) = \alpha_l^{-1}\{1 + 1/KC_i\}, \quad \text{Langmuir isotherm} \quad (6)$$

$$(v_0 - v_i)/v_0 = Z\alpha_l\{\ln C_0 + \ln C_i\}, \quad \text{Temkin isotherm} \quad (7)$$

where v_0 and v_i are the step velocities in the absence and presence of impurities, respectively; α_l is an effectiveness factor for impurity adsorption at the kink site as a function of supersaturation. When the adsorption site is the surface terrace, the step velocity is related to the impurity concentration as[18−19]

$$\{v_0/(v_0 - v_i)\}^2 = \alpha_s^{-2}\{1 + 1/KC_i\}, \quad \text{Langmuir isotherm} \quad (8)$$

$$\{(v_0 - v_i)/v_0\}^2 = Z\alpha_s^2\{\ln C_0 + \ln C_i\}, \quad \text{Temkin isotherm} \quad (9)$$

the face growth rate R is related to the nucleation rate J and the step velocity v as

$$R \propto J^{1/3} v^{2/3} \quad (10)$$

eqs 6−9 may be described, using R, as follows when J is constant regardless of the impurity concentration:

$$R_0^{3/2}/(R_0^{3/2} - R_i^{3/2}) = \alpha_l^{-1}\{1 + 1/KC_i\},$$
Langmuir kink model (11)

$$\{R_0^{3/2}/(R_0^{3/2} - R_i^{3/2})\}^2 = \alpha_s^{-2}\{1 + 1/KC_i\},$$
Langmuir terrace model (12)

$$(R_0^{3/2} - R_i^{3/2})/R_0^{3/2} = Z\alpha_l\{\ln C_0 + \ln C_i\},$$
Temkin kink model (13)

$$\{(R_0^{3/2} - R_i^{3/2})/R_0^{3/2}\}^2 = Z\alpha_s^2\{\ln C_0 + \ln C_i\},$$
Temkin terrace model (14)

where R_0 and R_i are face growth rates in the absence and presence of impurities, respectively.

The adsorption of magnesium and zinc was well described by the Langmuir kink model. The plots of $R_0^{3/2}/(R_0^{3/2} - R_i^{3/2})$ (eq 11) showed linear dependence on $1/C_i$ in the whole range

TABLE 1: Adsorption Constants of Magnesium and Zinc for the HAP *c*-face at pH 7.4 and at 25 °C

adsorption mechanism	impurity	concentration	K or C_0 (L/mol)
Langmuir kink model	Mg	<1.5 mM	1.97×10^4
kink model	Zn	<7.5 μM	2.13×10^6
Temkin kink model	Mg	<0.15 mM	1.12×10^5
kink model	Mg	>0.15 mM	1.10×10^{12}
kink modyel	Zn	<3.0 μM	1.67×10^7
kink model	Zn	>3.0 μM	1.82×10^{13}
Temkin terrace model	Mg	<0.15 mM	4.38×10^4
terrace model	Mg	>0.15 mM	2.26×10^8
terrace model	Zn	<3.0 μM	7.13×10^6
terrace model	Zn	>3.0 μM	1.95×10^9

on $1/C_i$ (Figures 7a and 7b). The adsorption constants for the Langmuir kink model were calculated as $K_{mg} = 1.97 \pm 0.3 \times 10^4$ L/mol ($\alpha_l^{-1} = 1.14$) and $K_{zn} = 2.13 \pm 0.3 \times 10^6$ L/mol ($\alpha_l^{-1} = 1.00$).

On the other hand, in the Temkin isotherm, the plots of $(R_0^{3/2} - R_i^{3/2})/R_0^{3/2}$ and $\{(R_0^{3/2} - R_i^{3/2})/R_0^{3/2}\}^2$ against ln C_i showed the presence of flexion points at a magnesium concentration of 0.15 mM and a zinc concentration of 3.0 μM (Figures 7c,d). Each linear part has a different Temkin adsorption constant. All adsorption constants for Langmuir and Temkin isotherms are listed in Table 1.

Discussion

The Langmuir kink model showed linear correlation for both magnesium and zinc (Figures 7c,d), although the Langmuir terrace model showed nonlinear correlation. The Temkin kink and terrace models showed linear correlation with flexion points (Figures 7c,d). Therefore, it is concluded that the mechanism of the inhibitory effect of magnesium and zinc best follows the Langmuir kink model. However, if the chemical composition and/or structure of impurity species changes with their concentration, activation energies for adsorption and physical or chemical bonding between the species and the *c*-face surface could also change with concentration. In this case, flexion points may appear in the relationship described by eqs 13 and 14, as shown in Figures 7c,d.

The AFM observation was consistent with the Langmuir kink model. In the Langmuir kink model, the impurities adsorb at the kink sites of the step front and inhibit the growth. AFM images demonstrated a decrease in diameter of the two-dimensional islands with an increase in magnesium or zinc concentration. This decrease indicated a reduction in the velocity of lateral advancement of step fronts of the two-dimensional islands due to the adsorption of the impurities.

In the Langmuir kink model, the coverage θ was calculated (eq 4) as $\theta_{mg} = 0.94$ ($C_{mg} = 1.5$ mM) and $\theta_{zn} = 0.90$ ($C_{zn} = 7.5$ μM). In the case of zinc, 90% of kinks were poisoned at the zinc concentration of 7.5 μM, and the growth of the *c*-face was almost completely inhibited (Figure 3b). In the case of magnesium, despite 94% of kinks being poisoned at a magnesium concentration of 1.5 mM, growth still proceeded with a growth rate of about 2×10^{-2} nm/s (Figure 3a). This suggests that magnesium was detached from the HAP surface into the solution after adsorption, or that magnesium was partially incorporated into calcium sites in the HAP structure.

The roughness of the step front of two-dimensional islands is estimated as follows. The value α_l in eq 6 can be calculated from the results in Figures 7a and 7b, and is given as[18]

$$\alpha_l = \gamma a/\ln(1 + \sigma)kT\chi_0 \qquad (15)$$

growth unit, k is the Boltzmann constant, T is the absolute temperature, and χ_0 is the average distance between kinks, respectively. The edge free energy for the HAP *c*-face was found to be $\gamma = 3.3\ kT$ in our previous study.[14] χ_0 is estimated as $\chi_0 \approx a$ for the HAP *c*-face, which suggests that the edge of two-dimensional islands on the *c*-face is rough. This indicates that a relatively high concentration of impurities is required to poison the kink sites, inducing the reduction of the lateral growth of two-dimensional islands. Considering that zinc inhibited the growth of the *c*-face more effectively and completely than magnesium (Figure 3), the considerable difference in inhibitory effect between magnesium and zinc may indicate the difference in the size of chemical species of impurities when they adsorb on the *c*-face. It is thus assumed that magnesium and zinc adsorbed in the form of free magnesium ions and the zinc phosphate compound such as $Zn_3(PO_4)_2 \cdot 4H_2O$ (hopeite), respectively, as presented in the previous report.[6] Since the molecular size of hopeite is much larger than the size of a free cation, it can poisoned several kinks at the same time. This assumption is supported by the calculation of supersaturation with respect to magnesium phosphate and zinc phosphate. The solubility products for $Mg_3(PO_4)_2$ and $Zn_3(PO_4)_2 \cdot 4H_2O$ are $10^{-23.98}$ and $10^{-35.29}$, respectively.[20,21] The supersaturation of solutions used were from -0.99 to -0.76 with respect to $Mg_3(PO_4)_2$ and from -0.85 to 0.63 with respect to $Zn_3(PO_4)_2 \cdot 4H_2O$, respectively.[21,22] Since magnesium phosphate is more soluble than the zinc phosphate compound, magnesium is more likely to take the form of free cations as compared with zinc, in the present study.

On the other hand, zinc may show an inhibitory effect regardless of the size of chemical species of impurities. In our recent study, it was revealed by ab initio calculation that $Zn_3(PO_4)_2$ exists stably with two Zn−O bond lengths of 2.04 and 1.77 Å, whereas each $Ca_3(PO_4)_2$ or $Mg_3(PO_4)_2$ has only one bond length, 2.30 Å (Ca−O) or 2.03 Å (Mg−O).[23] The Zn−O bond length of 1.77 Å is obviously shorter than that of Ca−O. Indeed, it was found experimentally that two Zn−O bond lengths coexist in the hopeite structure. The mean bond lengths (Zn−O) are 2.099 and 1.963 Å reported in ref 24 and 2.106 and 1.949 Å reported in ref 25. Each longer or shorter length is found in the ZnO_6 octahedron or ZnO_4 tetrahedron, respectively. On the other hand, calcium in the HAP structure are octahedrally coordinated to oxygen atoms from phosphate with a mean bond length of 2.36 Å (Ca−O).[26] Zinc takes a tetrahedral coordination more easily than calcium, due to the smaller ionic radius of zinc than that of calcium.[27] Therefore, the structural mismatch occurs between zinc phosphate and HAP when zinc ion combines with phosphate on the HAP surface. This structural mismatch causes the large inhibitory effect of zinc and completely inhibits the growth of the *c*-face. In contrast, magnesium in $Mg_3(PO_4)_2 \cdot 8H_2O$ are octahedrally coordinated to oxygen atoms from phosphate with mean bond lengths of 2.08 Å (Mg−O).[28] This means that a serious structural mismatch may not occur, even though a magnesium ion combines with phosphate on the HAP surface. Although whitlockite was not a major growing phase as mentioned in a result section, it may be possible that whitlockite is formed as an inhibitor in magnesium containing solutions. In this case, however, the situation is the same as explained above. Since calcium in whitlockite is octahedrally coordinated to oxygen atoms from phosphate as well as calcium in HAP, a serious structural mismatch between whitlockite and growing HAP should not

DOCKET ALARM

Explore Litigation Insights

Docket Alarm provides insights to develop a more informed litigation strategy and the peace of mind of knowing you're on top of things.

Real-Time Litigation Alerts

Keep your litigation team up-to-date with **real-time alerts** and advanced team management tools built for the enterprise, all while greatly reducing PACER spend.

Our comprehensive service means we can handle Federal, State, and Administrative courts across the country.

Advanced Docket Research

With over 230 million records, Docket Alarm's cloud-native docket research platform finds what other services can't. Coverage includes Federal, State, plus PTAB, TTAB, ITC and NLRB decisions, all in one place.

Identify arguments that have been successful in the past with full text, pinpoint searching. Link to case law cited within any court document via Fastcase.

Analytics At Your Fingertips

Learn what happened the last time a particular judge, opposing counsel or company faced cases similar to yours.

Advanced out-of-the-box PTAB and TTAB analytics are always at your fingertips.

API

Docket Alarm offers a powerful API (application programming interface) to developers that want to integrate case filings into their apps.

LAW FIRMS
Build custom dashboards for your attorneys and clients with live data direct from the court.

Automate many repetitive legal tasks like conflict checks, document management, and marketing.

FINANCIAL INSTITUTIONS
Litigation and bankruptcy checks for companies and debtors.

E-DISCOVERY AND LEGAL VENDORS
Sync your system to PACER to automate legal marketing.